

# **A Novel Framework for Molecular Characterization of Atmospherically Relevant Organic Compounds Based on Collision Cross Section and Mass-to-Charge Ratio**

X. Zhang<sup>1</sup>, J. E. Krechmer<sup>2,3</sup>, M. Groessl<sup>4</sup>, W. Xu<sup>1</sup>, S. Graf<sup>4</sup>, M. Cubison<sup>4</sup>,  
J. T. Jayne<sup>1</sup>, J.L. Jimenez<sup>2,3</sup>, D. R. Worsnop<sup>1</sup>, and M. R. Canagaratna<sup>1</sup>

<sup>1</sup> Center for Aerosol and Cloud Chemistry, Aerodyne Research Inc., Billerica, MA 01821, USA

<sup>2</sup> Department of Chemistry and Biochemistry, University of Colorado, Boulder, CO 80309, USA

<sup>3</sup> Cooperative Institute for Research in Environmental Sciences, Boulder, CO 80309, USA

<sup>4</sup> TOFWERK, CH-3600 Thun, Switzerland

*Correspondence to:* M. R. Canagaratna (mrcana@aerodyne.com)

1 **Abstract**

2 A new metric is introduced for representing the molecular signature of  
3 atmospherically relevant organic compounds, the collision cross section ( $\Omega$ ), a quantity  
4 that is related to the structure and geometry of molecules and is derived from ion mobility  
5 measurements. By combination with the mass-to-charge ratio ( $m/z$ ), a two-dimensional  
6  $\Omega - m/z$  space is developed to facilitate the comprehensive investigation of the complex  
7 organic mixtures. A unique distribution pattern of chemical classes, characterized by  
8 functional groups including amine, alcohol, carbonyl, carboxylic acid, ester, and organic  
9 sulfate, is developed on the 2-D  $\Omega - m/z$  space. Species of the same chemical class,  
10 despite variations in the molecular structures, tend to situate as a narrow band on the  
11 space and follow a trend line. Reactions involving changes in functionalization and  
12 fragmentation can be represented by the directionalities along or across these trend lines,  
13 thus allowing for the interpretation of atmospheric transformation mechanisms of organic  
14 species. The characteristics of trend lines for a variety of functionalities that are  
15 commonly present in the atmosphere can be predicted by the core model simulations,  
16 which provide a useful tool to identify the chemical class to which an unknown species  
17 belongs on the  $\Omega - m/z$  space. Within the band produced by each chemical class on the  
18 space, molecular structural assignment can be achieved by utilizing collision induced  
19 dissociation as well as by comparing the measured collision cross sections in the context  
20 of those obtained via molecular dynamics simulations.

21

22

23

24

25

26

27

## 28 1. Introduction

29 Organic species in the atmosphere — their chemical transformation, mass transport,  
30 and phase transitions — are essential for the interaction and coevolution of life and  
31 climate (Pöschl and Shiraiwa, 2015). Organic species are released into the atmosphere  
32 through biogenic processes and anthropogenic activities. Once in the atmosphere,  
33 organic species actively evolve via multiphase chemistry and gas-particle phase  
34 conversion. The complexity and dynamic behaviors of organic species have prevented  
35 our capability to accurately predict their levels, temporal and spatial variability, and  
36 oxidation dynamics associated with the formation and evolution of organic aerosols in the  
37 atmosphere.

38 Several two-dimensional frameworks have been developed in an effort to deconvolve  
39 the complexity of organic mixtures and visualize their atmospheric transformations. The  
40 Van Krevelen diagram, which cross plots the hydrogen-to-carbon atomic ratio (H:C) and  
41 the oxygen-to-carbon atomic ratio (O:C), has been widely used to represent the bulk  
42 elemental composition and the degree of oxygenation of organic aerosol (Heald et al.,  
43 2010). The average carbon oxidation state ( $\overline{OS}_C$ ), a quantity that necessarily increases  
44 upon oxidation, can be estimated from the elemental ratios (Kroll et al., 2011). When  
45 coupled with carbon number ( $n_C$ ), it provides constraints on the chemical composition of  
46 organic mixture and defines key classes of atmospheric processes based on the unique  
47 trajectory of the evolving organic chemical composition on the  $\overline{OS}_C - n_C$  space. The  
48 degree of oxidation has also been combined with the volatility (expressed as the effective  
49 saturation concentration,  $C^*$ ), forming a 2-D volatility basis set to describe the coupled  
50 aging and phase partitioning of organic aerosol (Donahue et al., 2012). These three  
51 spaces are designed to represent fundamental properties of the organic mixtures and  
52 provide insight into their chemical evolution in the atmosphere. Organic species span  
53 large varieties in the physicochemical properties. Species of similar volatility or  
54 elemental composition can differ vastly in structures and functionalities. One weakness of  
55 these frameworks is that they do not provide information on the organic components at  
56 molecular level.

57 In this article we introduce a new framework that is based on the collision cross  
58 section ( $\Omega$ ), a quantity that is related to the structure and geometry of a molecule. The  
59 collision cross section of a charged molecule determines its mobility as it travels through  
60 a neutral buffer gas such as  $N_2$  under the influence of a weak and uniform electric field.  
61 Species with open conformation undergo more collisions with buffer gas molecules and  
62 hence travel more slowly than the compact ones (Shvartsburg et al., 2000; Eiceman et al.,  
63 2013). Mobility measurements are usually performed with an Ion Mobility Spectrometer  
64 (IMS), where ions are separated mainly on the basis of their size, geometry, and  
65 subsequent interactions with the buffer gas. The combination of IMS with a Mass  
66 Spectrometer (MS) allows for further selection of ions based on their mass-to-charge  
67 ratios. The resulting IMS-MS plot provides separation of molecules according to two  
68 different properties: geometry (as reflected by the collision cross section) and mass (as  
69 reflected by the mass-to-charge ratio) (Kanu et al., 2008). The Ion Mobility Spectrometry  
70 - Mass Spectrometry (IMS-MS) analytical technique has been widely employed in the  
71 fields of biochemistry (McLean et al., 2005; Liu et al., 2007; Dwivedi et al., 2008;  
72 Roscioli et al., 2013; Groessl et al., 2015) and homeland security (Eiceman and Stone,  
73 2004; Ewing et al., 2001; Fernandez-Maestre et al., 2010). To our knowledge, the  
74 application of IMS-MS to study organic species in the atmosphere, however, has only  
75 been explored very recently (Krechmer et al., 2016).

76 We propose a two-dimensional collision cross section vs. mass-to-charge ratio ( $\Omega -$   
77  $m/z$ ) space to facilitate the comprehensive investigation of complex organic mixtures in  
78 the atmosphere. Despite the typical complexity of the detailed molecular mechanism  
79 involved in the atmospheric oxidation of organics molecules, they can be characterized  
80 by the distinctive functional groups attached to the carbon backbone (Zhang and Seinfeld,  
81 2013). We show that the investigated organic classes ( $m/z < 600$ ), characterized by  
82 functional groups including amine, alcohol, carbonyl, carboxylic acid, ester, and organic  
83 sulfate, exhibit unique distribution patterns on the  $\Omega - m/z$  space. Species of the same  
84 chemical class, despite variations in the molecular structures, tend to develop a narrow  
85 band and follow a trend line on the space. Reactions involving changes in  
86 functionalization and fragmentation can be represented by directionalities along or across  
87 these trend lines. The locations and slopes of the measured trend lines are shown to be

88 predicted by the core model (Mason et al., 1972), which characterizes the ion-neutral  
89 interactions as elastic sphere collisions. Within the narrow band produced by each  
90 chemical class on the  $\Omega - m/z$  space, molecular structural assignment is achieved with  
91 the assistance of collision induced dissociation analysis. Measured collision cross  
92 sections are also shown to be consistent with theoretically predicted values from the  
93 trajectory method (Mesleh et al., 1996; Shvartsburg and Jarrold, 1996) and are used to  
94 identify isomers that are separated from an isomeric mixture.

95

## 96 **2. Collision Cross Section Measurements**

### 97 2.1 Materials

98 A collection of chemical standards (ACS grade,  $\geq 96\%$ , purchased from Sigma  
99 Aldrich, St. Louis, MO, USA), classified as amines, alcohols, carbonyls, carboxylic  
100 acids, esters, phenols, and organic sulfates, were used to characterize the performance of  
101 IMS-MS. These chemicals were dissolved in an HPLC-grade solvent consisting of a 70%  
102 methanol / 29% water with 1% formic acid, at a concentration of approximately 10  $\mu\text{M}$ .

### 103 2.2 Instrumentation

104 Ion mobility measurements were performed using an Electrospray Ionization (ESI)  
105 Drift-Tube Ion Mobility Spectrometer (DT-IMS) interfaced to a Time-of-Flight Mass  
106 Spectrometer (TOFMS). The instrument was designed and manufactured by TOFWERK  
107 (Switzerland), with detailed descriptions and schematics provided by several recent  
108 studies (Kaplan et al., 2010; Zhang et al., 2014; Groessl et al., 2015; Krechmer et al.,  
109 2016). In the next few paragraphs, we will present the operating conditions of the ESI-  
110 IMS-TOFMS instrument.

111 Solutions of chemical standards were delivered to the ESI source via a 250  $\mu\text{L}$  gas-  
112 tight syringe (Hamilton, Reno, NV, USA) held on a syringe pump (Harvard Apparatus,  
113 Holliston, MA, USA) at a flow rate of 1  $\mu\text{L min}^{-1}$ . A deactivated fused silica capillary  
114 (360  $\mu\text{m}$  OD, 50  $\mu\text{m}$  ID, 50 cm length, New Objective, Woburn, MA, USA) was used as  
115 the sample transfer line. The ESI source was equipped with an uncoated SilicaTip Emitter  
116 (360  $\mu\text{m}$  OD, 50  $\mu\text{m}$  ID, 30  $\mu\text{m}$  tip ID, New Objective, Woburn, MA, USA) and

117 connected to the capillary through a conductive micro union (IDEX Health & Science,  
118 Oak Harbor, WA, USA). The charged droplets generated at the emitter tip migrate  
119 through a desolvation region in nitrogen atmosphere at room temperature, where ions  
120 evaporate from the droplets and are introduced into the drift tube through a Bradbury-  
121 Nielsen ion gate located at the entrance. The ion gate was operated in the Hadamard  
122 Transform mode, with a closure voltage of  $\pm 50$  V and an average gate pulse frequency of  
123  $1.2 \times 10^3$  Hz. The drift tube was held at a constant temperature ( $340 \pm 3$  K) and atmospheric  
124 pressure ( $\sim 1019$  mbar). A counter flow of  $N_2$  drift gas was introduced at the end of the  
125 drift region at a flow rate of  $1.2$  L  $min^{-1}$ . Ion mobility separation was carried out at a  
126 typical field strength of  $300 - 400$  V  $cm^{-1}$ , resulting in a reduced electric field of  
127 approximately  $1.4 - 1.8$  Td. After exiting from the drift tube, ions were focused into  
128 TOFMS through a pressure-vacuum interface that includes two segmented quadrupoles  
129 that were operated at  $\sim 2$  mbar and  $\sim 5 \times 10^{-3}$  mbar, respectively. Collision Induced  
130 Dissociation (CID) of parent ions is achieved by adjusting the voltages on the ion optical  
131 elements between the two quadrupole stages (Kaplan et al., 2010).

132 The ESI-IMS-TOFMS instrument was operated in the  $m/z$  range of 40 to 1500 with a  
133 total recording time of 90 s for each dataset. The Mass Spectrometer was calibrated using  
134 a mixture of quaternary ammonium salts, reserpine, and a mixture of fluorinated  
135 phosphazines (Ultramark 1621) in the positive mode and ammonium phosphate, sodium  
136 dodecyl sulfate, sodium taurocholate hydrate, and Ultramark 1621 in the negative mode.  
137 The ion mobility measurements were calibrated using tetraethyl ammonium chloride as  
138 the instrument standard and 2,4-lutidine as the mobility standard, as defined shortly  
139 (Fernández-Maestre et al., 2010). Mass spectra and ion mobility spectra were recorded  
140 using the acquisition package “Acquility” (v2.1.0, <http://www.tofwerk.com/acquility>).  
141 Post-processing was performed using the data analysis package “Tofware” (version 2.5.3,  
142 [www.tofwerk.com/tofware](http://www.tofwerk.com/tofware)) running in the Igor Pro (Wavemetrics, OR, USA)  
143 environment.

144 2.3 Calculations

145 The average velocity of an ion in the drift tube ( $v_d$ ) is proportional to its characteristic  
146 mobility constant ( $K / \text{cm}^2 \text{V}^{-1} \text{s}^{-1}$ ) and the electric field intensity ( $E_d$ ), provided that the  
147 field is weak (McDaniel and Mason, 1973):

148 
$$v_d = K E_d \quad (1)$$

149 Experimentally, ion mobility constants can be approximated from the time of ion clouds  
150 spent in the drift tube ( $t_d / \text{s}$ ), given by the rearranged form of Equation (1):

151 
$$t_d = \frac{1}{K} \frac{L_d^2}{V_d} \quad (2)$$

152 where  $L_d$  (cm) is the length of the drift tube and  $V_d$  (V) is the drift voltage. In the present  
153 study, drift time measurements were carried out at six different drift voltages ranging  
154 from 5 kV to 8 kV in  $\sim 1019 \text{ mbar}$  of nitrogen gas at 340 K (Figure S1 in the  
155 supplement). The ion mobility constant ( $K$ ) is derived by linear regression of the recorded  
156 arrival time ( $t_a$ ) of the ion clouds at the detector versus the reciprocal drift voltage:

157 
$$t_a = \frac{L_d^2}{K} \frac{1}{V_d} + t_0 \quad (3)$$

158 Note that the arrival time was determined from the centroid of the best-fit Gaussian  
159 distribution, see Figure S2 in the Supplement. The y-intercept of the best-fit line  
160 represents the transport time of the ion from the exit of the drift tube to the MS detector  
161 ( $t_0$ ), which exhibits strong  $m/z$  dependency that is attributable to a time-of-flight  
162 separation in the ion optics, see Figure S3 in the Supplement.

163 It is practical to discuss an ion's mobility in terms of the reduced mobility constant  
164 ( $K_0$ ), defined as:

165 
$$K_0 = K \frac{273.15}{T} \frac{P}{1013.25} \quad (4)$$

166 where  $P$  (mbar) is the pressure in the drift region and  $T$  (K) is the buffer gas temperature.  
167 In theory, the parameter  $K_0$  is constant for a given ion in a given buffer gas and can be  
168 used to characterize the intrinsic interactions of that particular ion-molecule pair. In  
169 practice, however,  $K_0$  values from different measurements might not be in good

170 agreement, primarily due to uncertainties in instrumental parameters such as  
 171 inhomogeneities in drift temperature and voltage (Fernández-Maestre et al., 2010). In  
 172 view of these uncertainties, the instrument standard is needed to provide an accurate  
 173 constraint on the instrumental parameters, such as voltage, drift length, pressure, and  
 174 temperature.

$$175 \quad K_0 \times t_d = \frac{L_d^2}{V_d} \frac{P}{1013.25} \frac{273.15}{T} = C_i \quad (5)$$

176 Tetraethyl ammonium chloride (TEA) is used here as the instrument standard, as its  
 177 reduced mobility is not affected by contaminants in the buffer gas (Fernández-Maestre et  
 178 al., 2010). Given the well-known  $K_0$  and measured  $t_d$  of the protonated TEA ion ( $m/z =$   
 179 130), Equation (5) yields an instrument constant  $C_i$  to calibrate the IMS performance.

180 Unlike TEA, the reduced mobility of species that are more likely to cluster with  
 181 contaminants can be significantly affected by impurities of the buffer gas. This category  
 182 of species can be used as a ‘mobility standard’ to qualitatively indicate the potential  
 183 contamination in the buffer gas. 2,4-Lutidine, with a well-characterized  $K_0$  value of 1.95  
 184  $\text{cm}^2 \text{V}^{-1} \text{s}^{-1}$ , is used as such a mobility standard. As shown Figure S4 in the Supplement,  
 185 the measured mobility of 2,4-Lutidine is 1.5% lower than its theoretical value, indicative  
 186 of the absence of contaminations in the buffer gas.

187 In the low field limit, the collision cross section of an ion ( $\Omega$ ) with a buffer gas is  
 188 related to its reduced mobility ( $K_0$ ) through the modified zero field (so called Mason-  
 189 Schamp) equation (McDaniel and Mason, 1973; Siems et al., 2012):

$$190 \quad \Omega = \frac{3ze}{16N_0} \left( \frac{2\pi}{k_B \mu T_0} \right)^{1/2} \frac{1}{K_0} \left[ 1 + \left( \frac{\beta_{MT}}{\alpha_{MT}} \right)^2 \left( \frac{v_d}{v_T} \right)^2 \right]^{-1/2} \quad (6a)$$

191 where  $z$  is the net number of integer charges on the ion,  $e$  is the elementary charge,  $N_0$  is  
 192 the number density of buffer gas at 273 K and 1013 mbar,  $k_B$  is the Boltzmann constant,  
 193  $\mu$  is the reduced mass for the molecule-ion pair,  $T_0$  is the standard temperature,  $v_d$  is the  
 194 drift velocity given by Equation (1),  $v_T$  is the thermal velocity, and  $\alpha_{MT}$  and  $\beta_{MT}$  are  
 195 correction coefficients for collision frequency and momentum transfer, respectively,  
 196 given by:



197 
$$\alpha_{\text{MT}} = \frac{2}{3} [1 + \hat{m}f_c + \hat{M}f_h] \quad \beta_{\text{MT}} = \left[ \frac{2}{\hat{m}(1 + \hat{m})} \right]^{1/2} \quad (7)$$

198 where  $\hat{m}$  and  $\hat{M}$  are molecular mass fractions of the ion and buffer gas molecule,  
 199 respectively, and  $f_c$  and  $f_h$  are the fractions of collisions in the cooling and heating classes,  
 200 respectively. Note that the reduced electric field used in this study is maximized at  $\sim 2$   
 201 Td, at which the drift velocity of any given ion is  $\sim$  two orders magnitude lower than its  
 202 thermal velocity, thus the values for  $f_c$  and  $f_h$  are assigned to be 0.5 and 0.5, respectively.  
 203 As all measurements in this study were carried out with nitrogen as the buffer gas, the  
 204 reported collision cross sections will be referred to  $\Omega_{\text{N}_2}$ . Matlab codes for calculating  $\Omega_{\text{N}_2}$   
 205 are given in the Supplement. Experimental  $\Omega_{\text{N}_2}$  values for a selection of ionic species are  
 206 consistent with those reported in literatures (see Table S1 in the Supplement).

207

### 208 **3. Collision Cross Section Modeling**

209 Kinetic theory indicates that the quantity  $\Omega$  is an orientationally averaged collision  
 210 integral ( $\Omega_{\text{avg}}^{(1,1)}$ ), which depends on the nature of ion-neutral interaction potential  
 211 (McDaniel and Mason, 1973). Given the potential, the collision integral can be calculated  
 212 through successive integrations over collision trajectories, impact parameters and energy.  
 213 Here we adopt two computational methods, i.e., trajectory method and core model, to  
 214 simulate the average collision integral. The trajectory method is a rigorous calculation of  
 215  $\Omega_{\text{avg}}^{(1,1)}$  by propagating classical trajectories of neutral molecules in a realistic neutral/ion  
 216 potential consisting of a sum of pairwise Lennard-Jones interactions and ion induced  
 217 dipole interactions (Mesleh et al., 1996; Shvartsburg and Jarrold, 1996). The core model  
 218 treats the polyatomic ion as a rigid sphere where the center of charge is displaced from  
 219 the geometry center. The ion-neutral interaction is approximately represented by the cross  
 220 section of two rigid spheres during elastic collisions. The potential during interaction  
 221 includes a long-range attraction term and a short-range repulsion term (Mason et al.,  
 222 1972).

223 The two models employed here represent opposite directions in the  $\Omega_{\text{avg}}^{(1,1)}$  computation  
 224 methods. The trajectory method is a rigorous calculation of  $\Omega_{\text{avg}}^{(1,1)}$  in a realistic

225 intermolecular potential yet the computation is time consuming. The core model, on the  
226 other hand, substantially simplifies the calculation of  $\Omega_{\text{avg}}^{(1,1)}$  as rigid sphere collisions at the  
227 expense of simulation accuracy. We will show shortly that the core model is used for  
228 locating individual chemical classes on the 2-D  $\Omega_{\text{N}_2} - m/z$  space. Within the band  
229 developed by each chemical class, molecular structure information can be deduced by  
230 comparing the measured collision cross section with those calculated by the trajectory  
231 method.

### 232 3.1 Trajectory Method

233 Molecular structures for L-leucine and D-isoleucine were initially constructed by  
234 Avogadro v1.1.1 (Hanwell et al., 2012). For each molecule, both protonation and  
235 deprotonation sites are created by placing a positive charge on the N-terminal amino  
236 group and a negative charge on the C-terminal carboxyl group, respectively. The  
237 geometry of each ion is further optimized using the Hartree-Fock method with the 6-  
238 31G(d,p) basis set via GAMESS (Schmidt et al., 1993). Partial atomic charges were  
239 estimated using Mulliken population analysis.

240 A freely available software, MOBCAL, developed by Jarrold and coworkers  
241 (<http://www.indiana.edu/~nano/software.html>) was used for computing the collision  
242 integrals. The potential term employed in the trajectory method takes the form:

$$243 \quad \Phi(\theta, \phi, \gamma, b, r) = 4\epsilon \sum_i^n \left[ \left( \frac{\sigma}{r_i} \right)^{12} - \left( \frac{\sigma}{r_i} \right)^6 \right] - \frac{\alpha_p}{2} \left( \frac{ze}{n} \right)^2 \left[ \left( \sum_i^n \frac{x_i}{r_i^3} \right)^2 + \left( \sum_i^n \frac{y_i}{r_i^3} \right)^2 + \left( \sum_i^n \frac{z_i}{r_i^3} \right)^2 \right] \quad (8)$$

244 where  $\theta$ ,  $\phi$ , and  $\gamma$  are three angles that define the geometry of ion-neutral collision,  $b$  is  
245 the impact parameter,  $\epsilon$  is the depth of the potential well,  $\sigma$  is the finite distance at which  
246 the interaction potential is zero,  $\alpha_p$  is the polarizability of the neutral, which is  $1.710 \times 10^{-}$   
247  $^{24} \text{cm}^3$  for  $\text{N}_2$  (Olney et al., 1997),  $n$  is the number of atoms in the ion, and  $r_i$ ,  $x_i$ ,  $y_i$ , and  $z_i$   
248 are coordinates that define the relative positions of individual atoms with respect to the  
249 buffer gas. Values of the Lenard-Jones parameters,  $\epsilon$  and  $\sigma$ , are taken from the universal  
250 force field (Casewit et al., 1992). The ion-quadrupole interaction and the orientation of  $\text{N}_2$   
251 molecule are not considered here (Kim et al., 2008; Campuzano et al., 2012).

252 3.2 Core Model

253 The core model, consisting of a (12-4) central potential displaced from the origin, is  
 254 used to represent interactions of polyatomic ions with N<sub>2</sub> molecules (Mason et al., 1972).  
 255 The (12-4) central potential includes a repulsive  $r^{-12}$  term, which describes the Pauli  
 256 repulsion at short ranges due to overlapping electron orbitals, as well as an attractive  $r^{-4}$   
 257 term, which describes attractions at long ranges due to ion induced dipole:

$$258 \quad \Phi(r) = \frac{\epsilon}{2} \left\{ \left( \frac{r_m - a}{r - a} \right)^{12} - 3 \left( \frac{r_m - a}{r - a} \right)^4 \right\} \quad (9)$$

259 where  $r$  is the distance between the ion-neutral geometric centers,  $a$  is the location of the  
 260 ionic center of charge measured from the geometrical center of the ion, and  $r_m$  is the  
 261 value of  $r$  at the potential minimum. At temperature of 0 K, the *polarization potential* can  
 262 be expressed as:

$$263 \quad \Phi_{\text{pol}}(r) = -\frac{e^2 \alpha_p}{2r^4} \quad (10)$$

264

265 where  $\alpha_p$  is the polarizability of the neutral. Thus  $\epsilon$  is given by:

$$266 \quad \epsilon = \frac{e^2 \alpha_p}{3(r_m - a)^4} \quad (11)$$

267 The collision cross section can be expressed in dimensionless form by extracting its  
 268 dependence on  $r_m$ :

$$269 \quad \Omega = \Omega^{(1,1)*} \pi r_m^2 \quad (12)$$

270 Tabulations of the dimensionless collision integral ( $\Omega^{(1,1)*}$ ) can be found in literatures  
 271 (Mason et al., 1972) as a function of dimensionless temperature ( $T^*$ ) and core diameter  
 272 ( $a^*$ ), given by:

$$273 \quad T^* = \frac{kT}{\epsilon} = \frac{3kT(r_m - a)^4}{e^2 \alpha_p} \quad a^* = \frac{a}{r_m} \quad (13)$$

274 Polynomial interpolation of the tabulated  $\Omega^{(1,1)*}$  yielded an analytical expression of the  
 275 collision cross section, with  $r_m$  and  $a$  as adjustable parameters. This expression was then

276 fit to the ion mobility datasets measured in N<sub>2</sub> buffer gas using a nonlinear least-square  
277 regression procedure (Matlab code is available upon request) (Johnson et al., 2004; Kim  
278 et al., 2005; Kim et al., 2008). Best-fit parameters,  $r_m$  and  $a$ , along with predicted vs.  
279 measured collision cross section are given in Table S2 in the Supplementary Information.

280

## 281 **4. Collision Cross Section vs. Mass-to-Charge Ratio 2-D Space**

### 282 4.1 Distribution of *multi*-Functional Organic Species

283 Figure 1 (A) shows the distribution of organic species, classified as (*di/poly/sugar*)-  
284 alcohol, *tertiary*-amine, *quaternary*-ammonium, (*mono/di*)-carbonyl, (*mono/di/tri*)-  
285 carboxylic acid, (*di*)-ester, organic sulfate, and *multi*-functional compounds, on the  
286 collision cross section vs. mass-to-charge ratio ( $\Omega_{N_2} - m/z$ ) 2-D space. One feature of the  
287 distribution pattern is that species with higher density as pure liquids and carbon  
288 oxidation state tend to occupy the lower region of the  $\Omega_{N_2} - m/z$  space. This is not  
289 surprising given that molecules of smaller collision cross sections tend to be much  
290 denser, and potentially more functionalized, than those with extended and open  
291 geometries. Furthermore, species of the same chemical class tend to occupy a narrow  
292 region and follow a trend line on the  $\Omega_{N_2} - m/z$  space. These observations form the basis  
293 of potentially utilizing locations and trends on the 2-D space to identify chemical classes  
294 to which an unknown compound belongs.

295 Small molecules ( $m/z < 200$ ) with similar size and geometry are situated closely  
296 together, as visualized by the ‘overlaps’ on the space. Improved visual separation of the  
297 species within the overlapping region is obtained by transforming  $\Omega_{N_2}$  to a quantity  
298  $\Delta\Omega_{N_2}$ , defined as the percentage difference between the measured collision cross section  
299 for any given molecular ion and the calculated projection area for a rigid spherical ion-N<sub>2</sub>  
300 pair with the same molecular mass. Since this idealized ion-N<sub>2</sub> pair does not account for  
301 interaction potentials and molecular conformation, it is only used as a reference state to  
302 improve visualization of the  $\Omega_{N_2} - m/z$  2-D space, as shown in Figure 1 (B).

## 303 4.2 $\Omega_{N_2} - m/z$ Trend Lines

304 The  $\Omega_{N_2} - m/z$  trend line visualized on the 2-D space describes the intrinsic increase  
305 in collision cross sections resulting from the increase in molecular mass by extending the  
306 carbon backbone or adding functional groups. It has been used for conformation space  
307 separation of different classes of biomolecules including lipids, peptides, carbohydrates,  
308 and nucleotides (McLean et al., 2005). Here we demonstrate for the first time the  
309 presence of trend lines for small molecules of atmospheric interest, and the trend line  
310 pattern for each chemical class can be predicted by the core model simulations.

311 Figure 2 shows the measured  $\Omega_{N_2}$  as a function of mass-to-charge ratio for (A)  
312 *tertiary-amine* and *quaternary-ammonium*, (B) (*di/poly/sugar*)-alcohol, and (C)  
313 (*mono/oxo/hydroxy*)-carboxylic acid. Also shown are the predicted  $\Omega_{N_2}$  by the core  
314 model, with adjustable parameters optimized by the measured  $\Omega_{N_2}$  for the subcategory  
315 spanning the largest  $m/z$  range in each chemical class. Specifically, *quaternary-*  
316 *ammonium*, propylene glycol, and *alkanoic-acid* are used in constraining the core model  
317 performance to predict the  $\Omega_{N_2} - m/z$  trend lines for amines, alcohols, and carboxylic  
318 acids. Species in each chemical class, regardless of the variety in the carbon skeleton  
319 structure, occupy a narrow range and appear along a  $\Omega_{N_2} - m/z$  trend line. Such a  
320 relationship can be further demonstrated by the goodness of the core model predictions,  
321 i.e., the difference between predicted and measured  $\Omega_{N_2}$  for compounds that are not used  
322 to optimize the core model performance. For amine series, predicted  $\Omega_{N_2}$  values for  
323 lutidine and pyridine are 8.2% and 0.8% higher, respectively, than the measurements. For  
324 alcohol series, the best-fit  $\Omega_{N_2} - m/z$  trend line constrained by propylene glycol can be  
325 used to predict the distribution of sugars and polyols within 3.5% difference on the space.  
326 For carboxylic acid series, hydroxyl-hexadecanoic acid falls closely on the predicted  
327  $\Omega_{N_2} - m/z$  trend line, despite the presence of an alcohol group on the  $C_{16}$  carbon chain.  
328 Predicted  $\Omega_{N_2}$  values for *oxo*-carboxylic acids are 4.4% – 6.1% lower than the  
329 observations. Benzoic acid exhibits a relatively large measurement-prediction gap (6.7%)  
330 potentially due to the presence of an aromatic ring.

331 The demonstrated  $\Omega_{N_2} - m/z$  trend lines provide a useful tool for categorization of  
332 structurally related compounds. Mapping out the locations and distribution patterns for  
333 various functionalities on the 2-D space would therefore facilitate classification of  
334 chemical classes for unknown compounds. It is likely that trend lines extracted from a  
335 complex organic mixture overlap and, as a result, the distribution pattern of unknowns on  
336 the space alone would not provide sufficient information on their molecular identities. In  
337 this case, the fragmentation pattern of unknowns upon collision induced dissociation  
338 (CID) needs to be explored for the functionality identification, as discussed in detail in  
339 Section 4.4. As it is highly unlikely that two distinct molecules will produce identical  
340 IMS, MS, as well as CID-based MS spectra, the 2-D framework therefore virtually  
341 ensures reliable identification of species of atmospheric interest.

#### 342 4.3 Trajectories for Atmospheric Transformation Processes

343 Functionalization (the addition of oxygen-containing functional groups) and  
344 fragmentation (the oxidative cleavage of C–C bonds) are key processes during  
345 atmospheric transformation of organics. Reactions involving changes in functionalization  
346 and fragmentation can be represented by directionalities on the  $\Omega_{N_2} - m/z$  space, as  
347 illustrated by the distribution pattern of carboxylic acids in Figure 3. Addition of one  
348 carbon atom always leads to an increase in mass and collision cross section, with a  
349 generic slope of approximately  $5 \text{ \AA}^2/\text{Th}$ . Although the addition of one oxygen atom in the  
350 form of a carbonyl group results in a similar increase in the molecular mass, it leads to a  
351 shallower slope compared with that from expanding the carbon chain. Addition of  
352 carboxylic or hydroxyl groups does not necessarily lead to an increase in the collision  
353 cross section, as the formation of the intramolecular hydrogen bonding ( $\text{O} - \text{H} \cdots \text{O}^-$ )  
354 could result in a more compact conformation of the molecule. In general, fragmentation  
355 moves materials to the bottom left and functionalization to the right on the space.

#### 356 4.4 Molecular Structure Elucidation of *multi*-Functional Species

357 The demonstrated  $\Omega_{N_2} - m/z$  relationship provides a useful tool to identify the  
358 chemical class to which an unknown species belongs. To further identify its molecular  
359 structure, knowledge on the electrospray ionization mechanism for the generation of

360 *quasi*-molecular ions, as well as fragmentation patterns of the molecular ion upon  
361 collision induced dissociation (CID), is required.

362 For species investigated in this study, their integral molecular structures are  
363 maintained during electrospray ionization. An exhibition of molecular formulas of ionic  
364 species is given in Table 1. Depending on the proton susceptibility of functional groups,  
365 amines, esters, and aromatic aldehydes are sensitive to the ESI(+) mode, whereas  
366 carboxylic acids and organic sulfates yield high signal-to-noise ratios in the ESI(-)  
367 spectra. Specifically, the positive mass spectra collected for amines and amino acids  
368 show major ions at  $m/z$  values corresponding to the protonated cations ( $[M+H]^+$ ).  
369 Sodiated clusters ( $[M+Na]^+$ ) of esters were observed as the dominant peak in the ESI(+)  
370 spectra. Aromatic aldehydes combine with a methyl group ( $[M+CH_3]^+$ ) via the gas-phase  
371 aldol reaction between protonated aldehydes and methanol in the positive mode. Sugars  
372 and polyols can be readily ionized in both positive and negative mode with the addition  
373 of a proton or sodium ion or deprotonation. Extensive formation of oligomers is observed  
374 from the positive mass spectra of propylene glycol, with the deprotonated propanol ( $-$   
375  $OCH_2CH(CH_3)-$ ) as the primary building block. Monoanions ( $[M-H]^-$ ) were exclusively  
376 observed in the negative mass spectra of (*mono/di/tri/multi*)-carboxylic acids due to the  
377 facile ionization afforded by the carboxylic group. It is worth noting that quantification of  
378 these species requires prior chromatographic separation to avoid matrix suppression on  
379 the analyte of interest (Zhang et al., 2016) or alternative ionization scheme that is  
380 compatible with the high-voltage IMS inlet and does not induce matrix effects.

381 The instrument used in this study enables the collision induced dissociation of the  
382 abovementioned precursor ions after ion mobility separation but prior to the mass  
383 spectrometer (IMS-CID-MS). As a consequence, product ions exhibit the identical  
384 mobility (drift time) with that of the precursor ion. IMS-CID-MS spectra for individual  
385 compounds are then generated by the extraction of “mobility-selected” MS spectra that  
386 contain both precursor and fragments. The major advantage of this approach is that it is  
387 possible to obtain fragmentation spectra for all precursor ions simultaneously. This is in  
388 contrast to MS/MS techniques which require the isolation of a small mass window prior  
389 to fragmentation which can be a problem for very complex samples or time-resolved  
390 analysis. Figure 4 shows the measured drift time for the precursor and product ions

391 generated from species representative of amines, aldehydes, carboxylic acids, esters, and  
392 nitro compounds. Collision induced dissociation patterns of these species are used to  
393 elucidate the fragmentation mechanisms for corresponding functional groups. The  
394 deprotonated carboxylic acid is known to undergo facile decarboxylation to produce a  
395 carbanion. If additional carboxylic groups are present in the molecule, combined loss of  
396 water and carbon dioxide is expected (Grossert et al., 2005). Alternatively, the presence  
397 of an –OH group adjacent to the carboxylic group would usually result in a neutral loss of  
398 formic acid (Greene et al., 2013), see the fragmentation pattern for 16-  
399 hydroxyhexadecanoic acid as an illustration. Scission of the C–O bond in the ester  
400 structure or the C–O bond between the secondary/tertiary carbon and the alcoholic  
401 oxygen is observed for the ester series examined, consistent with previous studies (Zhang  
402 et al., 2015). A primary fragmentation resulting in loss of CO was evident in the spectrum  
403 of methylate derivative of protonated carbonyls ( $\text{RCHOCH}_3^+$ ) (Neta et al., 2014). The  
404 IMS-CID-MS spectrum of deprotonated 4-nitrophenol is shown as a representative of  
405 organic nitro compounds. Two dominant peaks at  $m/z$  108 and  $m/z$  92 are observed,  
406 resulting from the neutral loss of NO and NO<sub>2</sub>, respectively.

407 Signal intensities of the fragments from the CID pathway of the precursor ion depend  
408 on the collision voltage, as shown in Figure 5. At low collision voltages, the precursor  
409 ions predominate with transmission optimized at approximately 5 V potential gradient.  
410 As the collision voltage increases, the intensity of the precursor ion decreases and that of  
411 each product ion increases, eventually reaching a maximum level, and then decreases due  
412 to subsequent fragmentation. The dependence of the product ion abundance on the  
413 collision voltage provides information on the relative strength of the covalent bond at  
414 which the parent molecule fragments. Consequently, the energy required to induce a  
415 certain fragmentation pathway could potentially also serve as an additional parameter for  
416 structure elucidation. For example, the predominance of the product ion at  $m/z$  149  
417 suggests that cleavage of the carbonyl-oxygen bond in the ester moiety is the dominant  
418 fragmentation pathway upon CID of dioctyl phthalate ( $\text{C}_{24}\text{H}_{38}\text{O}_4$ ).



## 419 4.5 Resolving Isomeric Mixtures

420 Here we demonstrate the separation of isomers on the  $\Omega_{N_2} - m/z$  space using the  
421 mixture of L-leucine and D-isoleucine as an illustration, as they can be directly ionized  
422 by electrospray in both positive and negative modes due to the presence of amino and  
423 carboxyl groups. We refer the reader to Krechmer et al. (2016) for the mobility separation  
424 of atmospheric relevant isomeric species. Figure 6 (A and B) shows a single peak that  
425 corresponds to the protonated ( $[M+H]^+$ ,  $m/z = 132$ ) and deprotonated ( $[M-H]^-$ ,  $m/z =$   
426 130) forms of the leucine mixture, respectively, in the positive and negative MS spectra.  
427 Upon further separation based on their distinct mobility in the  $N_2$  buffer gas, the leucine  
428 mixture is clearly resolved in the positive mode, while a broad peak is observed in the  
429 negative ion mobility spectrum, see Figure 6 (C and D). Note that a typical IMS resolving  
430 power ( $t/dt_{50}$ ) of 100 leads to a baseline separation of leucine isomers that differ by 0.3  
431 ms in the measured drift time. Figure 6 (E-H) shows the IMS spectra for individual  
432 leucine isomeric configurations, which provide precise constraints for the peak  
433 assignment in the leucine mixture. Also given here are the measured vs. predicted  
434 collision cross sections for each isomer, with predictions lower by 3.3 ~ 6.9% compared  
435 with the measurements. However, despite the underprediction, the model using trajectory  
436 method correctly predicts the relative collision cross sections of the isomers and therefore  
437 also the order in which they appear in the IMS spectrum. The underprediction of  $\Omega_{N_2}$   
438 may result from the simplification that linear  $N_2$  molecules are considered as elastic and  
439 specular spheres in the current model configuration (Larriba-Andaluz and Hogan Jr,  
440 2014). Further development of the model to more appropriately predict  $\Omega_{N_2}$  values is  
441 needed.

442

## 443 5. Conclusions

444 We propose a new metric, collision cross section ( $\Omega$ ), for characterizing organic  
445 species of atmospheric interest. Collision cross section represents an effective interaction  
446 area between a charged molecule and neutral buffer gas as it travels through under the  
447 action of a weak electric field, and thus relates to the chemical structure and 3-D  
448 conformation of this molecule. The collision cross section of individual molecular ions is

449 calculated from the ion mobility measurements using an Ion Mobility Spectrometer. In  
450 this study, we provide the derived  $\Omega_{N_2}$  values for a series of organic species including  
451 amines, alcohols, carbonyls, carboxylic acids, esters, organic sulfates, and *multi-*  
452 functional compounds.

453 The collision cross section, when coupled with mass-to-charge ratio, provides a 2-D  
454 framework for characterizing the molecular signature of atmospheric organic  
455 components. The  $\Omega_{N_2} - m/z$  space is employed to guide our fundamental understanding  
456 of chemical transformation of organic species in the atmosphere. We show that different  
457 chemical classes tend to develop unique narrow bands with trend lines on the  $\Omega_{N_2} - m/z$   
458 space. Trajectories associated with atmospheric transformation mechanisms either cross  
459 or follow these trend lines through the space. The demonstrated  $\Omega_{N_2} - m/z$  trend lines  
460 provide a useful tool for resolving various functionalities in the complex organic mixture.  
461 These intrinsic trend lines can be predicted by the core model, which provides a guide for  
462 locating unknown functionalities on the  $\Omega_{N_2} - m/z$  space.

463 Within each band that that belongs to a particular chemical class on the space, species  
464 can be further separated based on their distinct structures and geometries. We  
465 demonstrate the utility of collision induced dissociation technique, upon which the  
466 resulted product ions share the identical drift time as the precursor ion, to facilitate the  
467 elucidation of molecular structures of organic species. We employ the  $\Omega_{N_2} - m/z$   
468 framework for separation of isomeric mixtures as well by comparing the measured  
469 collision cross sections with those predicted using the trajectory method. Further  
470 advances in algorithms to correctly predict collision cross sections *ab initio* from  
471 molecular coordinates are therefore also expected to significantly improve identification  
472 of unknowns.

473

#### 474 **Acknowledgement**

475 This study was supported by the U.S. National Science Foundation (NSF)  
476 Atmospheric and Geospace Sciences (AGS) grants 1537446. J.E.K. was supported by  
477 fellowships from CIRES and EPA STAR (FP-91770901-0). J.L.J. was supported by DOE

478 (BER/ASR) DE-SC0011105 and EPA STAR 83587701-0. This manuscript has not been  
479 reviewed by EPA and thus no endorsement should be inferred.

480

481 **Appendix:**

482  $a$  (Å): the location of the ionic center of charge from the geometrical center of the ion.

483  $a^*$ : the dimensionless core diameter.

484  $\alpha_{MT}$ : the correction coefficient for collision frequency.

485  $\alpha_p$  (cm<sup>3</sup>): the polarizability of the neutral.

486  $\beta_{MT}$ : the correction coefficient for momentum transfer.

487  $C_i$ : the instrument constant that is used to calibrate the IMS performance.

488  $\epsilon$  (eV): the depth of the potential well.

489  $E_d$  (V/cm): the electric field intensity in the drift tube.

490  $\Phi$  (eV): the ion-neutral interaction potential.

491  $f_c$ : the fraction of collisions in the cooling classes.

492  $f_h$ : the fraction of collisions in the heating classes.

493  $k_B$  (m<sup>2</sup> kg s<sup>-2</sup> K<sup>-1</sup>): Boltzmann constant.

494  $K$  (cm<sup>2</sup> V<sup>-1</sup> s<sup>-1</sup>): the characteristic mobility constant of a given ion.

495  $K_0$  (cm<sup>2</sup> V<sup>-1</sup> s<sup>-1</sup>): the reduced mobility constant of a given ion.

496  $L_d$  (V/cm): the length of the drift tube.

497  $\hat{m}$ : the mass fraction of the ion in the ion-molecule pair.

498  $\hat{M}$ : the mass fraction of the buffer gas molecule (N<sub>2</sub>) in the ion-molecule pair.

499  $m/z$  (Th): the mass-to-charge ratio of any given ion.

500  $N_0$  (# cm<sup>-3</sup>): the number density of buffer gas at 273 K and 1013 mbar.

501  $\Omega$  (Å<sup>2</sup>): the collision cross section.

502  $\Omega_{N_2}$  (Å<sup>2</sup>): the collision cross section using N<sub>2</sub> as the buffer gas.

503  $\Omega_{avg}^{(1,1)}$ : the orientationally averaged collision integral.

504  $\Omega^{(1,1)*}$ : the dimensionless collision integral.

505  $P$  (mbar): the pressure in the drift region.

506  $r$  (Å): the distance between the ion-neutral geometric centers.

507  $r_m$  (Å): the value of  $r$  at the potential minimum.

508  $\sigma$  (Å): the finite distance at which the interaction potential is zero.  
509  $T$  (K): the buffer gas temperature.  
510  $T_0$  (K): the standard temperature.  
511  $T^*$ : the dimensionless temperature.  
512  $t_a$  (s): the recorded arrival time of the ion clouds at the detector.  
513  $t_d$  (s): the time of ion clouds spent in the drift tube.  
514  $t_0$  (s): the transport time of ion clouds from the exit of the drift tube to the MS detector.  
515  $v_d$  (s): the average velocity of an ion in the drift tube.  
516  $v_T$  (m s<sup>-1</sup>): the thermal velocity.  
517  $V_d$  (V): the voltage applied to the drift tube.  
518  $z$ : the net number of integer charges on the ion.

519

## 520 **References:**

521 Campuzano, I., Bush, M. F., Robinson, C. V., Beaumont, C., Richardson, K., Kim, H.,  
522 and Kim, H. I.: Structural characterization of drug-like compounds by ion mobility mass  
523 spectrometry: comparison of theoretical and experimentally derived nitrogen collision  
524 cross sections, *Anal. Chem.*, 84, 1026-1033, 2012.

525 Casewit, C. J., Colwell, K. S., and Rappe, A. K.: Application of a universal force field to  
526 organic molecules, *J. Am. Chem. Soc.*, 114, 10035-10046, 1992.

527 Donahue, N. M., Kroll, J. H., Pandis, S. N., and Robinson, A. L.: A two-dimensional  
528 volatility basis set—Part 2: Diagnostics of organic-aerosol evolution, *Atmos. Chem. Phys.*,  
529 12, 615-634, 2012.

530 Dwivedi, P., Wu, P., Klopsch, S. J., Puzon, G. J., Xun, L., and Hill Jr, H. H.: Metabolic  
531 profiling by ion mobility mass spectrometry (IMMS), *Metabolomics*, 4, 63-80, 2008.

532 Eiceman, G. A., and Stone, J. A.: Ion mobility spectrometers in national defence, *Anal.*  
533 *Chem.*, 76, 390-397, 2004.

534 Eiceman, G. A., Karpas, Z., and Hill Jr, H. H.: Ion mobility spectrometry, CRC press,  
535 2013.

536 Ewing, R. G., Atkinson, D. A., Eiceman, G. A., and Ewing, G. J.: A critical review of ion  
537 mobility spectrometry for the detection of explosives and explosive related compounds,  
538 *Talanta*, 54, 515-529, 2001.

539 Fernandez-Maestre, R., Harden, C. S., Ewing, R. G., Crawford, C. L., and Hill, H. H., Jr.:  
540 Chemical standards in ion mobility spectrometry, *Analyst*, 135, 1433-1442, 2010.

541 Fernández-Maestre, R., Harden, C. S., Ewing, R. G., Crawford, C. L., and Hill, H. H.:  
542 Chemical standards in ion mobility spectrometry, *Analyst*, 135, 1433-1442, 2010.

543 Greene, L. E., Grossert, J. S., and White, R. L.: Correlations of ion structure with  
544 multiple fragmentation pathways arising from collision-induced dissociations of selected  
545  $\alpha$ -hydroxycarboxylic acid anions, *J. Mass Spectrom.*, 48, 312-320, 2013.

546 Groessl, M., Graf, S., and Knochenmuss, R.: High resolution ion mobility-mass  
547 spectrometry for separation and identification of isomeric lipids, *Analyst*, 140, 6904-  
548 6911, 2015.

549 Grossert, J. S., Fancy, P. D., and White, R. L.: Fragmentation pathways of negative ions  
550 produced by electrospray ionization of acyclic dicarboxylic acids and derivatives, *Can. J.*  
551 *Chem.*, 83, 1878-1890, 2005.

552 Hanwell, M. D., Curtis, D. E., Lonie, D. C., Vandermeersch, T., Zurek, E., and  
553 Hutchison, G. R.: Avogadro: An advanced semantic chemical editor, visualization, and  
554 analysis platform, *J. Cheminform.*, 4, 10.1186/1758-2946-4-17, 2012.

555 Heald, C. L., Kroll, J. H., Jimenez, J. L., Docherty, K. S., DeCarlo, P. F., Aiken, A. C.,  
556 Chen, Q., Martin, S. T., Farmer, D. K., and Artaxo, P.: A simplified description of the  
557 evolution of organic aerosol composition in the atmosphere, *Geophys. Res. Lett.*, 37,  
558 L08803, 10.1029/2010GL042737, 2010.

559 Johnson, P. V., Kim, H. I., Beegle, L. W., and Kanik, I.: Electrospray ionization ion  
560 mobility spectrometry of amino acids: ion mobilities and a mass-mobility correlation, *J.*  
561 *Phys. Chem. A*, 108, 5785-5792, 2004.

562 Kanu, A. B., Dwivedi, P., Tam, M., Matz, L., and Hill, H. H.: Ion mobility-mass  
563 spectrometry, *J. Mass Spectrom.*, 43, 1-22, 2008.

564 Kaplan, K., Graf, S., Tanner, C., Gonin, M., Fuhrer, K., Knochenmuss, R., Dwivedi, P.,  
565 and Hill Jr, H. H.: Resistive Glass IM-TOFMS, *Anal. Chem.*, 82, 9336-9343, 2010.

566 Kim, H., Kim, H. I., Johnson, P. V., Beegle, L. W., Beauchamp, J. L., Goddard, W. A.,  
567 and Kanik, I.: Experimental and theoretical investigation into the correlation between  
568 mass and ion mobility for choline and other ammonium cations in N<sub>2</sub>, *Anal. Chem.*, 80,  
569 1928-1936, 2008.

570 Kim, H. I., Johnson, P. V., Beegle, L. W., Beauchamp, J. L., and Kanik, I.: Electrospray  
571 ionization ion mobility spectrometry of carboxylate anions: Ion mobilities and a mass-  
572 mobility correlation, *J. Phys. Chem. A*, 109, 7888-7895, 2005.

573 Krechmer, J. E., Groessl, M., Zhang, X., Junninen, H., Massoli, P., Lambe, A. T.,  
574 Kimmel, J. R., Cubison, M. J., Graf, S., Lin, Y. H., Budisulistiorini, S. H., Zhang, H.,  
575 Surratt, J. D., Knochenmuss, R., Jayne, J. T., Worsnop, D. R., Jimenez, J. L., and  
576 Canagaratna, M. R.: Ion Mobility Spectrometry-Mass Spectrometry (IMS-MS) for on-  
577 and off-line analysis of atmospheric gas and aerosol species, *Atmos. Meas. Tech.*, 9,  
578 3245-3262, 2016.

579 Kroll, J. H., Donahue, N. M., Jimenez, J. L., Kessler, S. H., Canagaratna, M. R., Wilson,  
580 K. R., Altieri, K. E., Mazzoleni, L. R., Wozniak, A. S., Bluhm, H., Mysak, E. R., Smith,  
581 J. D., Kolb, C. E., and Worsnop, D. R.: Carbon oxidation state as a metric for describing  
582 the chemistry of atmospheric organic aerosol, *Nature Chem.*, 3, 133-139, 2011.

583 Larriba-Andaluz, C., and Hogan Jr, C. J.: Collision cross section calculations for  
584 polyatomic ions considering rotating diatomic/linear gas molecules, *J. Chem. Phys.*, 141,  
585 194107, doi.org/10.1063/1.4901890, 2014.

586 Liu, X., Valentine, S. J., Plasencia, M. D., Trimpin, S., Naylor, S., and Clemmer, D. E.:  
587 Mapping the human plasma proteome by SCX-LC-IMS-MS, *J. Am. Soc. Mass*  
588 *Spectrom.*, 18, 1249-1264, 2007.

589 Mason, E. A., O'Hara, H., and Smith, F. J.: Mobilities of polyatomic ions in gases: core  
590 model, *J. Phys. B*, 5, 169-172, 1972.

591 McDaniel, E. W., and Mason, E. A.: *The mobility and diffusion of ions in gases*, Wiley,  
592 1973.

593 McLean, J. A., Ruotolo, B. T., Gillig, K. J., and Russell, D. H.: Ion mobility–mass  
594 spectrometry: a new paradigm for proteomics, *Int. J. Mass Spectrom.*, 240, 301-315,  
595 2005.

596 Mesleh, M. F., Hunter, J. M., Shvartsburg, A. A., Schatz, G. C., and Jarrold, M. F.:  
597 Structural information from ion mobility measurements: effects of the long-range  
598 potential, *J. Phys. Chem.*, 100, 16082-16086, 1996.

599 Neta, P., Simón - Manso, Y., Liang, Y., and Stein, S. E.: Loss of H<sub>2</sub> and CO from  
600 protonated aldehydes in electrospray ionization mass spectrometry, *Rapid Commun.*  
601 *Mass Spectrom.*, 28, 1871-1882, 2014.

602 Olney, T. N., Cann, N. M., Cooper, G., and Brion, C. E.: Absolute scale determination  
603 for photoabsorption spectra and the calculation of molecular properties using dipole sum-  
604 rules, *Chem. Phys.*, 223, 59-98, 1997.

605 Pöschl, U., and Shiraiwa, M.: Multiphase Chemistry at the Atmosphere–Biosphere  
606 Interface Influencing Climate and Public Health in the Anthropocene, *Chem. Rev.*, 115,  
607 4440-4475, 2015.

608 Roscioli, K. M., Zhang, X., Li, S. X., Goetz, G. H., Cheng, G., Zhang, Z., Siems, W. F.,  
609 and Hill, H. H.: Real time pharmaceutical reaction monitoring by electrospray ion  
610 mobility-mass spectrometry, *Int. J. Mass Spectrom.*, 336, 27-36, 2013.

611 Schmidt, M. W., Baldrige, K. K., Boatz, J. A., Elbert, S. T., Gordon, M. S., Jensen, J.  
612 H., Koseki, S., Matsunaga, N., Nguyen, K. A., and Su, S.: General atomic and molecular  
613 electronic structure system, *J. Comput. Chem.*, 14, 1347-1363, 1993.

614 Shvartsburg, A. A., and Jarrold, M. F.: An exact hard-spheres scattering model for the  
615 mobilities of polyatomic ions, *Chem. Phys. Lett.*, 261, 86-91, 1996.

616 Shvartsburg, A. A., Liu, B., Jarrold, M. F., and Ho, K.-M.: Modeling ionic mobilities by  
617 scattering on electronic density isosurfaces: Application to silicon cluster anions, *J.*  
618 *Chem. Phys.*, 112, 4517-4526, 2000.

619 Siems, W. F., Viehland, L. A., and Hill Jr, H. H.: Improved momentum-transfer theory  
620 for ion mobility. 1. Derivation of the fundamental equation, *Anal. Chem.*, 84, 9782-9791,  
621 2012.

622 Zhang, X., and Seinfeld, J. H.: A functional group oxidation model (FGOM) for SOA  
623 formation and aging, *Atmos. Chem. Phys.*, 13, 5907-5926, 2013.

624 Zhang, X., Knochenmuss, R., Siems, W. F., Liu, W., Graf, S., and Hill, H. H., Jr.:  
625 Evaluation of Hadamard transform atmospheric pressure ion mobility time-of-flight mass  
626 spectrometry for complex mixture analysis, *Anal. Chem.*, 86, 1661-1670, 2014.

627 Zhang, X., McVay, R. C., Huang, D. D., Dalleska, N. F., Aumont, B., Flagan, R. C., and  
628 Seinfeld, J. H.: Formation and evolution of molecular products in  $\alpha$ -pinene secondary  
629 organic aerosol, *Proc. Natl. Acad. Sci. USA*, 112, 14168-14173, 2015.

630 Zhang, X., Dalleska, N. F., Huang, D. D., Bates, K. H., Sorooshian, A., Flagan, R. C.,  
631 and Seinfeld, J. H.: Time-resolved molecular characterization of organic aerosols by  
632 PILS+ UPLC/ESI-Q-TOFMS, *Atmos. Environ.*, 130, 180-189, 2016.

633

Table 1. Overview of organic standards investigated in this study.

Class	Chemical	Molecular Formula	Ion		$\Omega_{N_2}$ ( $\text{\AA}^2$ )	Molecular Structure
			Formula	$m/z$		
Amine	Tetraethyl ammonium chloride	$C_8H_{20}NCl$	$[M-Cl]^+$	130.16	122.1	
	Tetrapropyl ammonium chloride	$C_{12}H_{28}NCl$	$[M-Cl]^+$	186.10	143.8	
	Tetrabutyl ammonium iodide	$C_{16}H_{36}NI$	$[M-I]^+$	242.17	165.8	
	Tetrapentyl ammonium chloride	$C_{20}H_{44}NCl$	$[M-Cl]^+$	298.35	190.0	
	Tetraheptyl ammonium chloride	$C_{28}H_{60}NCl$	$[M-Cl]^+$	410.47	236.5	
	2,4-Lutidine	$C_7H_9N$	$[M+H]^+$	108.08	123.4	
	2,6-Di-tert-butylpyridine	$C_{13}H_{21}N$	$[M+H]^+$	192.17	145.0	
Amino acid	L-Leucine	$C_6H_{13}NO_2$	$[M+H]^+$	132.10	137.8	
			$[M-H]^-$	130.09	144.4	
	D-Isoleucine	$C_6H_{13}NO_2$	$[M+H]^+$	132.10	135.2	
			$[M-H]^-$	130.09	140.3	
<i>mono</i> Carboxylic Acid	Benzoic acid	$C_7H_6O_2$	$[M-H]^-$	121.03	128.6	
	Octanoic acid	$C_8H_{16}O_2$	$[M-H]^-$	143.11	144.7	
	2-Butyloctanoic acid	$C_{12}H_{24}O_2$	$[M-H]^-$	199.17	162.0	
	Tridecanoic acid	$C_{13}H_{26}O_2$	$[M-H]^-$	213.19	166.2	$CH_3(CH_2)_{10}CH_2COOH$
	Pentadecanoic acid	$C_{15}H_{30}O_2$	$[M-H]^-$	241.22	173.7	$CH_3(CH_2)_{12}CH_2COOH$
	Palmitic acid	$C_{16}H_{32}O_2$	$[M-H]^-$	255.23	177.9	$CH_3(CH_2)_{13}CH_2COOH$
	Stearic acid	$C_{18}H_{36}O_2$	$[M-H]^-$	283.26	185.4	$CH_3(CH_2)_{15}CH_2COOH$
	Oleic acid	$C_{18}H_{34}O_2$	$[M-H]^-$	281.25	186.9	$CH_3(CH_2)_6CH_2CH=CH(CH_2)_7COOH$



<i>di/multi</i> Carboxylic Acid	Succinic acid	C <sub>4</sub> H <sub>6</sub> O <sub>4</sub>	[M-H] <sup>-</sup>	117.02	124.6	
	Glutaric acid	C <sub>5</sub> H <sub>8</sub> O <sub>4</sub>	[M-H] <sup>-</sup>	131.03	128.4	
	Adipic acid	C <sub>6</sub> H <sub>10</sub> O <sub>4</sub>	[M-H] <sup>-</sup>	145.05	131.5	
	Pimelic acid	C <sub>7</sub> H <sub>12</sub> O <sub>4</sub>	[M-H] <sup>-</sup>	159.06	134.0	
	Azelaic acid	C <sub>9</sub> H <sub>16</sub> O <sub>4</sub>	[M-H] <sup>-</sup>	187.09	143.5	
	Sebacic acid	C <sub>10</sub> H <sub>18</sub> O <sub>4</sub>	[M-H] <sup>-</sup>	201.11	148.9	
	1,2,3-Propane tricarboxylic acid	C <sub>6</sub> H <sub>8</sub> O <sub>6</sub>	[M-H] <sup>-</sup>	175.02	122.2	
	Cyclohexane tricarboxylic acid	C <sub>9</sub> H <sub>12</sub> O <sub>6</sub>	[M-H] <sup>-</sup>	215.06	135.0	
	Mellitic acid	C <sub>12</sub> H <sub>6</sub> O <sub>12</sub>	[M-H <sub>2</sub> O-H] <sup>-</sup>	322.96	154.6	
Ester	Dibutyl oxalate	C <sub>10</sub> H <sub>18</sub> O <sub>4</sub>	[M+Na] <sup>+</sup>	225.11	170.0	
	Dibutyl phtahlate	C <sub>16</sub> H <sub>22</sub> O <sub>4</sub>	[M+Na] <sup>+</sup>	301.14	192.4	
			[2M+Na] <sup>+</sup>	579.29	255.5	
	Diocetyl phthalate	C <sub>24</sub> H <sub>38</sub> O <sub>4</sub>	[M+H] <sup>+</sup>	391.28	203.6	
Alcohol	Propylene glycol	C <sub>3</sub> H <sub>8</sub> O <sub>2</sub>	[2M-2H <sub>2</sub> O+Na] <sup>+</sup>	215.12	144.8	
			[4M-3H <sub>2</sub> O+Na] <sup>+</sup>	273.17	156.4	
			[5M-4H <sub>2</sub> O+H] <sup>+</sup>	309.23	165.7	
			[5M-4H <sub>2</sub> O+Na] <sup>+</sup>	331.21	169.6	
			[6M-5H <sub>2</sub> O+H] <sup>+</sup>	367.27	179.1	
			[6M-5H <sub>2</sub> O+Na] <sup>+</sup>	389.24	181.6	
			[7M-6H <sub>2</sub> O+H] <sup>+</sup>	425.31	190.8	
			[7M-6H <sub>2</sub> O+Na] <sup>+</sup>	447.28	193.9	
			[8M-7H <sub>2</sub> O+H] <sup>+</sup>	483.35	204.7	
			[8M-7H <sub>2</sub> O+Na] <sup>+</sup>	505.32	206.2	
	[9M-8H <sub>2</sub> O+H] <sup>+</sup>	541.39	218.5			
	[9M-8H <sub>2</sub> O+Na] <sup>+</sup>	563.36	219.3			
	[10M-9H <sub>2</sub> O+H] <sup>+</sup>	599.42	231.3			
	[10M-9H <sub>2</sub> O+Na] <sup>+</sup>	621.40	231.8			

	DL-Threitol	C <sub>4</sub> H <sub>10</sub> O <sub>4</sub>	[M+Na] <sup>+</sup>	145.05	133.0	
	Xylitol	C <sub>5</sub> H <sub>12</sub> O <sub>5</sub>	[M-H] <sup>-</sup>	151.06	131.2	
	Sucrose	C <sub>12</sub> H <sub>22</sub> O <sub>11</sub>	[M-H] <sup>-</sup> [M+Na] <sup>+</sup>	341.11 365.11	167.6 175.1	
Carbonyl	Hexane-3,4-dione	C <sub>6</sub> H <sub>10</sub> O <sub>2</sub>	[M+H] <sup>+</sup> [M+CH <sub>3</sub> ] <sup>+</sup>	115.08 129.09	115.7 121.3	
	Acetophenone	C <sub>8</sub> H <sub>8</sub> O	[M+CH <sub>3</sub> ] <sup>+</sup>	135.08	120.4	
	Cinnamaldehyde	C <sub>9</sub> H <sub>8</sub> O	[M+CH <sub>3</sub> ] <sup>+</sup>	147.08	123.9	
<i>multi</i> Functional Compound	Levulinic acid	C <sub>5</sub> H <sub>8</sub> O <sub>3</sub>	[M-H] <sup>-</sup>	115.04	130.0	
	4-Acetylbutyric acid	C <sub>6</sub> H <sub>10</sub> O <sub>3</sub>	[M-H] <sup>-</sup>	129.06	134.5	
	Homovanillic acid	C <sub>9</sub> H <sub>10</sub> O <sub>4</sub>	[M-H] <sup>-</sup>	181.05	147.7	
	16-Hydroxy hexadecanoic acid	C <sub>16</sub> H <sub>32</sub> O <sub>3</sub>	[M-H] <sup>-</sup>	271.22	183.7	
	Oxaloacetic acid	C <sub>4</sub> H <sub>4</sub> O <sub>5</sub>	[M-H] <sup>-</sup>	131.06	118.3	
	Ketoglutaric acid	C <sub>5</sub> H <sub>6</sub> O <sub>5</sub>	[M-H] <sup>-</sup>	145.01	120.9	
	Oxoazelaic acid	C <sub>9</sub> H <sub>14</sub> O <sub>5</sub>	[M-H] <sup>-</sup>	201.08	133.3	
	Malic acid	C <sub>4</sub> H <sub>6</sub> O <sub>5</sub>	[M-H] <sup>-</sup>	133.01	111.4	
	Tartaric acid	C <sub>4</sub> H <sub>6</sub> O <sub>6</sub>	[M-H] <sup>-</sup>	149.01	116.0	
Citric acid	C <sub>6</sub> H <sub>8</sub> O <sub>7</sub>	[M-H] <sup>-</sup>	191.02	123.0		
Organic Sulfate	Sodium Dodecyl sulfate	C <sub>12</sub> H <sub>25</sub> SO <sub>4</sub> Na	[M-Na] <sup>-</sup>	265.15	163.6	
	Sodium Taurocholate	C <sub>26</sub> H <sub>44</sub> SO <sub>7</sub> NNa	[M-Na] <sup>-</sup>	514.28	206.4	

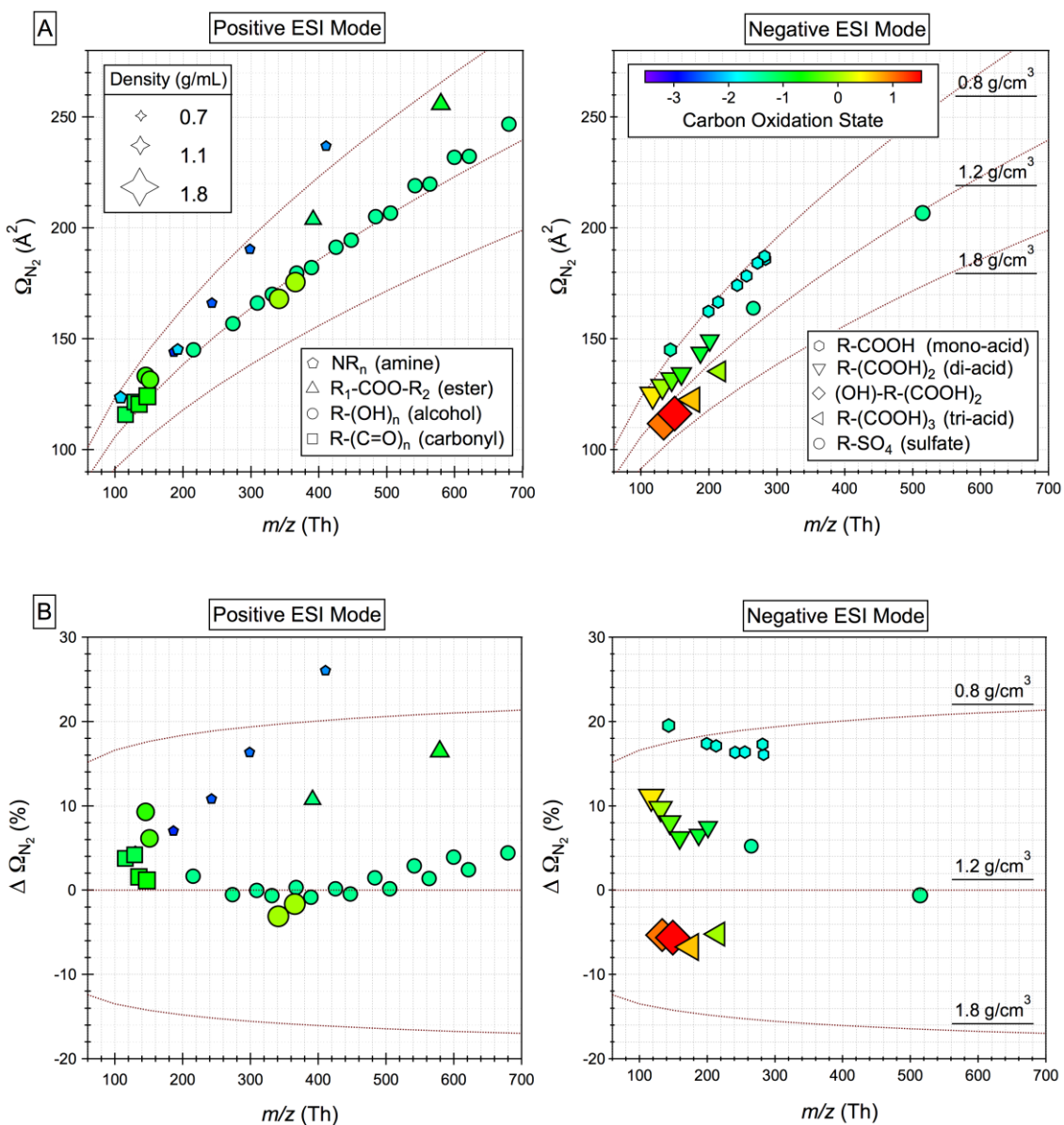


Figure 1. Distribution of organic species including alcohol ( $R-(OH)_n$ ,  $n = 2-8$ ), amine ( $NR_3$ ), *quaternary*-ammonium ( $NR_4$ ), carbonyl ( $R-(C=O)_n$ ,  $n = 1-2$ ), carboxylic acid ( $R-(COOH)_n$ ,  $n = 1-3$ ), ester ( $R_1-COO-R_2$ ), organic sulfate ( $R-SO_4$ ), and *multi*-functional compounds ( $(OH)-R-(COOH)_2$ ) on the (A)  $\Omega_{N_2} - m/z$  space and (B)  $\Delta\Omega_{N_2} - m/z$  space. Note that species that are detected in different ion modes (+/-) are plotted separately.

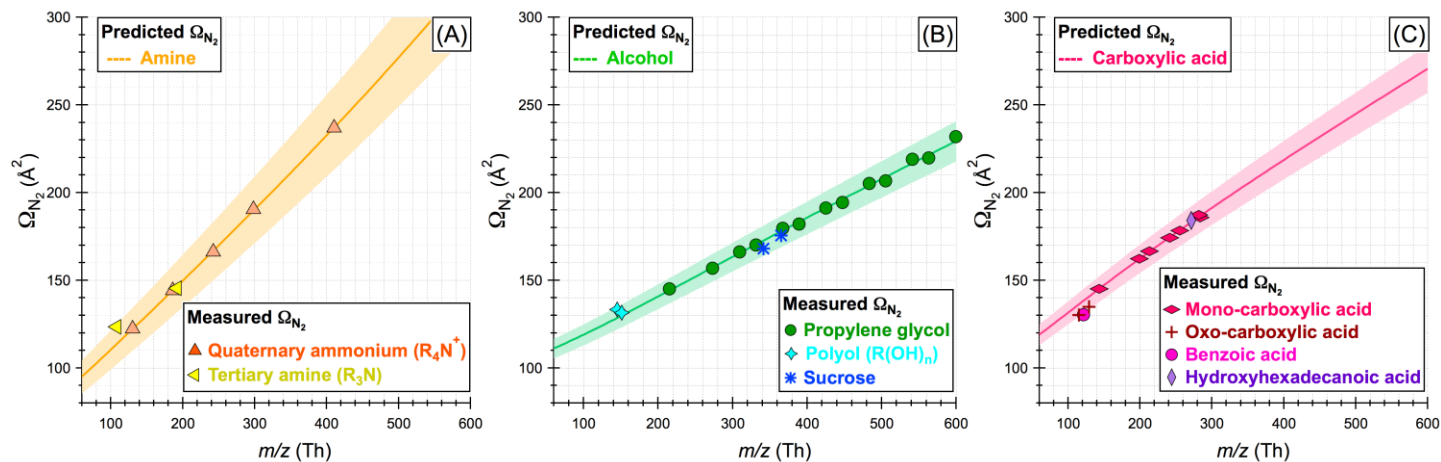


Figure 2. Measured collision cross sections ( $\Omega_{N_2}$ ) for (A) *tertiary*-amine and *quaternary*-ammonium, (B) (*di/poly/sugar*)-alcohol, and (C) (*mono/oxo/hydroxy*)-carboxylic acid as a function of the mass-to-charge ratio. Also shown are the predicted  $\Omega_{N_2} - m/z$  trend lines for amine, alcohol, and carboxylic acid by the core model. Here, *quaternary*-ammonium, propylene glycol, and  $C_8$ - $C_{18}$  *alkanoic*-acid are used to optimize the adjustable parameters in the core model (The markers are in the same color as the trend lines). The colored shade in each figure represents the maximum deviations (8.21%, 3.54%, and 6.69% for amine, alcohol, and carboxylic acid, respectively) of the predicted  $\Omega_{N_2}$  from the measured  $\Omega_{N_2}$  for species that are not used to constrain the core model. A single plot showing the separation of these three chemical classes is given in Figure S5 in the supplement.

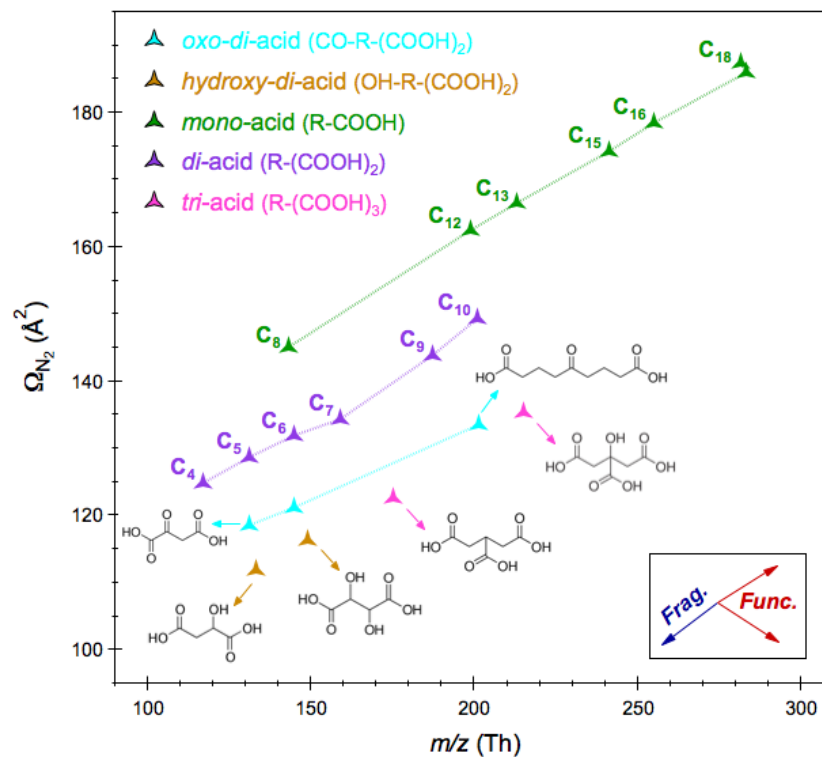


Figure 3. Trajectories associated with reactions involving functionalization (changes in the type and number of functional groups) and fragmentation (changes in the carbon chain length) through the 2-D  $\Omega_{N_2} - m/z$  space using carboxylic acid series as an illustration.

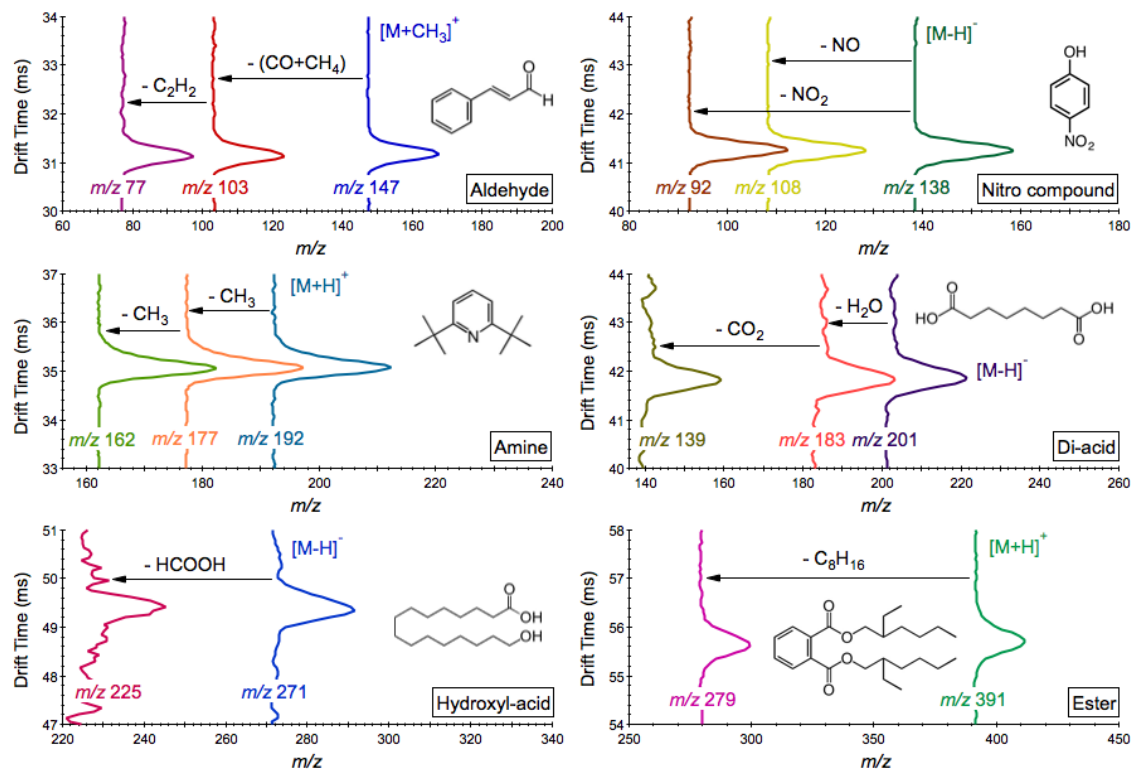


Figure 4. Collision induced dissociation patterns for molecular ions generated from cinnamaldehyde, diethyl phthalate, 2,6-di-tert-butylpyridine, 4-nitrophenol, 16-hydroxyhexadecanoic acid, and sebacic acid on the 2-D framework with mass-to-charge ratio on the  $x$ -axis and drift time on the  $y$ -axis. The corresponding mobility selected MS spectra for each species is given in Figure S6 in the supplement.

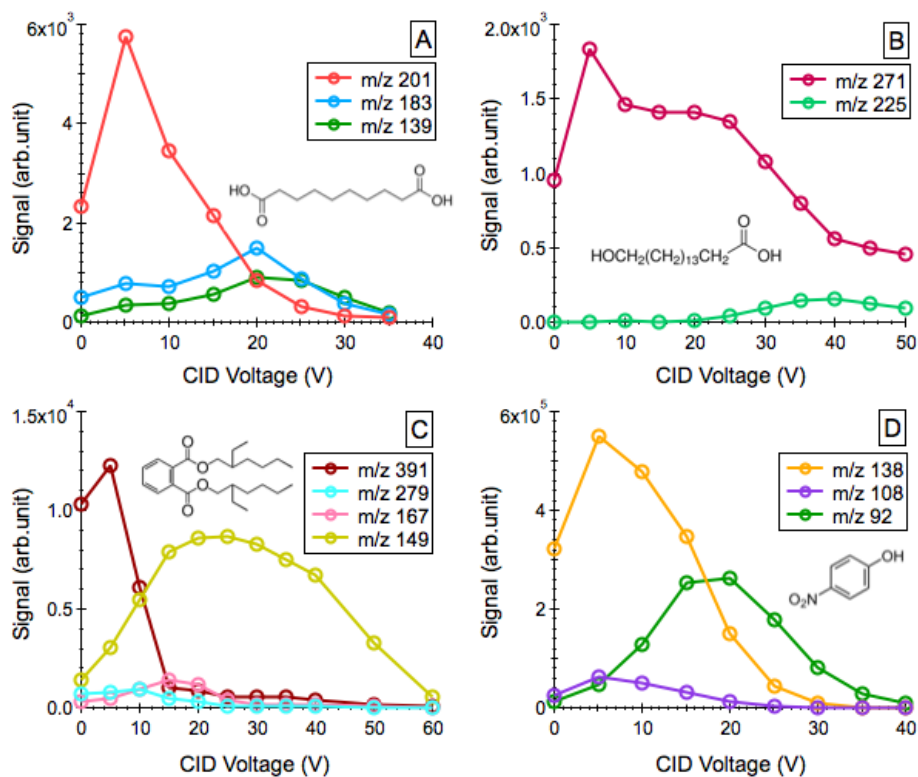


Figure 5. Product ion peak intensities as a function of collision voltage in the ‘mobility-selected’ MS spectra of (A) deprotonated sebacic acid, (B) deprotonated 16-hydroxyhexadecanoic acid, (C) sodiated dioctyl phthalate, and (D) deprotonated 4-nitrophenol.

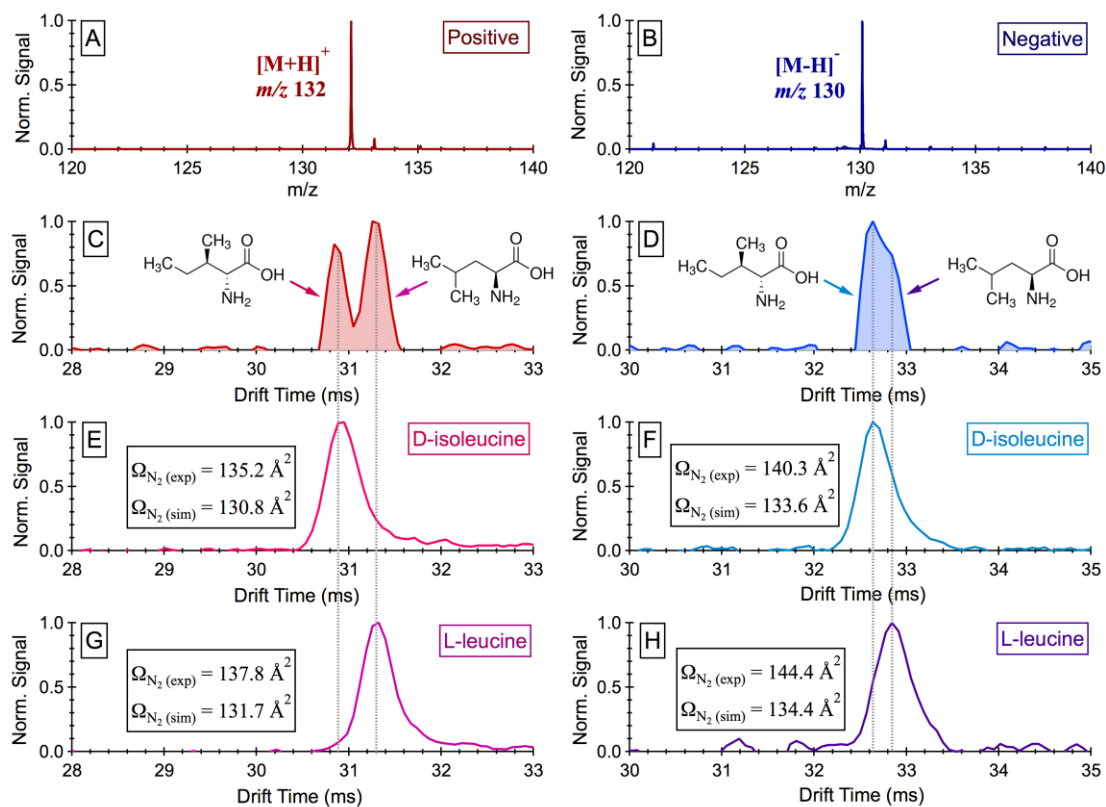


Figure 6. (A/B) ESI mass spectra collected for an equi-molar mixture (20  $\mu\text{M}$  each) of L-leucine and D-isoleucine in positive and negative mode. (C/D) Measured drift time distributions for the leucine mixture in positive and negative mode. (E/F) Measured vs. predicted  $\Omega_{N_2}$  for D-isoleucine, together with its drift time distributions in positive and negative mode. (G/H) Measured vs. predicted  $\Omega_{N_2}$  for L-leucine, together with its drift time distributions in positive and negative mode. Note that all measurements were performed at  $\sim 303 \text{ K}$  and  $\sim 1019 \text{ mbar}$  with an electric field strength of 414 and 403  $\text{V cm}^{-1}$  in the positive and negative mode, respectively.